This article has been accepted for inclusion in a future issue of this journal. Content is final as presented, with the exception of pagination.

A Dynamic Mode Decomposition Framework for Global Power System Oscillation Analysis

Emilio Barocio, *Member, IEEE*, Bikash C. Pal, *Fellow, IEEE*, Nina F. Thornhill, *Senior Member, IEEE*, and Arturo Roman Messina, *Fellow, IEEE*

***Abstract*—A global multiscale method based on a dynamic mode decomposition (DMD) algorithm to characterize the global behavior of transient processes recorded using wide-area sensors is proposed. The method interprets global dynamic behavior in terms of both, spatial patterns or shapes and temporal patterns associated with dynamic modes containing essentially single-frequency components, from which the mode shapes, frequencies and growth and decay rates of the modes can be extracted simultaneously. These modes are then used to detect the coherent and dominant structures within the data. The technique is well suited for fast wide-area monitoring and assessment of global instability in the context of modern data fusion-based estimation techniques. Results of the application of the proposed method to large, high-dimensional data sets are encouraging.**

***Index Terms*—Dynamic mode decomposition, inter-area oscillations, mode-shape.**

I. Introduction

POWER system dynamic monitoring for a near real-time control has received increased importance in the past 5–10 years because of two primary reasons. Firstly the analysis of the causes and mechanisms of several large blackouts identified the lack of fast and dynamic monitoring [1]. Secondly the phasor measurement technology (PMUs) for deployment over wide area power system is now available commercially. A successful wide-area monitoring of low-frequency oscillation requires adaptive global identification methods, which can accurately identify and track the evolving dynamics of critical system modes [2], [3].

The dynamic monitoring of systems should be robust, and resilient against uncharacteristic variation of signal information. The tools must operate in real-time to quickly quantify the risks to system shut down such as blackouts. In the past few large power system collapse it has been observed that slowly growing power oscillations of low frequency have triggered the final events. These are known as inter-area modes as they are manifested across several large utilities. Naturally fasts monitoring of these oscillations is way to commit control to avert such situations.

Identifying damping factors and the frequency of oscillations has been very popular to quantify the stability margin in small signal sense [4]. Both, model and data driven tools, are reported. The recently concluded IEEE Task Force on modal identification [3] summarizes recent work on this topic.

Inter area oscillations monitoring targeting temporal amplitudes and phases of inter-area mode and energy of oscillations are useful attributes to assess the proximity of the system to instability [5]–[13]. Because of their global nature, modal frequencies and modal speeds in particular, are directly associated with global system behavior and may therefore be useful to detect and visualize the stressed part of the system. In addition, the level of energy associated with the oscillations as a measure of stability margin is a useful indicator as it is robust against noise in the measured signal.

Recently, several multi-scale dynamic feature extraction methods have been used to objectively identify and extract dominant patterns exhibited by power system transient processes. Of these methods, proper orthogonal decomposition (POD) and principal component analysis (PCA) have been applied to identify dynamically coherent generators and mode shapes using ensembles of model simulations and measured data [5]–[7]. The simplicity of the model structure allows for direct numerical analysis of large data sets collected using strategically located sensors.

Over the last few years, data-driven methods for modal identification based on the use of the Koopman operator have been developed [8]–[10]. These methods use Arnoldi-like techniques and enable complex oscillatory processes to be represented by several single-frequency nonlinear modes from which oscillations and interacting generators could be identified. The application of this approach, however, is challenging due to both, the high dimensionality of the parameter space and the computational complexity.

In this paper, a physically-motivated dynamic mode decomposition (DMD) algorithm is introduced to monitor the spatial and temporal dynamics of nonlinear transient phenomena. Distinct from previous power system identification methods, the proposed framework allows the multi-scale spatial and temporal dynamics in observed data to be identified directly from observational data [14]–[18].

Methods for interpreting the nonlinear mathematical structure of the spatio-temporal model in terms of temporal and structural components are discussed and a physical interpretation is provided.

Manuscript received December 18, 2013; revised May 26, 2014 and August 21, 2014; accepted October 29, 2014. This work was supported by the Marie Curie FP7-IAPP Project "Using real-time measurements for monitoring and management of power transmission dynamics for the smart grid- REAL-SMART", Contract No. PIAP-GA 2009-251304. Paper no. TPWRS-01599-2013.

E. Barocio, B. C. Pal, and N. F. Thornhill are with Imperial College London, London, NE 68902, U.K. (e-mail: ebarocio@imperial.ac.uk; b.pal@imperial.ac.uk; n.thornhill@imperial.ac.uk).

A. R. Messina is with CINVESTAV, Guadalajara, AL 36849, Mexicao (e-mail: aroman@gdl.cinvestav.mx).

Color versions of one or more of the figures in this paper are available online at http://ieeexplore.ieee.org.

Digital Object Identifier 10.1109/TPWRS.2014.2368078

0885-8950 © 2014 IEEE. Personal use is permitted, but republication/redistribution requires IEEE permission.
See http://www.ieee.org/publications_standards/publications/rights/index.html for more information.

This article has been accepted for inclusion in a future issue of this journal. Content is final as presented, with the exception of pagination.

Studies on both, transient stability and measured data suggest that the method can accurately identify the dominant spatial and temporal structures in a large data set.

II. Spatio Temporal Analysis Methods

In this section, an overview of two related spatio-temporal analysis methods, Koopman mode analysis, and the proper orthogonal decomposition (POD) method is provided within the context of modal estimations.

A. Proper Orthogonal Decomposition

Assume that $x(\nu_j, t_i), j = 1, \ldots, m, i = 1, 2 \ldots l, \ldots, N$ denotes an element of observation, where ν_j is the jth grid or measurement point, and t_i is the time at which the observations are made. To introduce the proposed method, define the data matrix, $\boldsymbol{X}_1^N$, as

$$\boldsymbol{X}_1^N = \begin{bmatrix} \overbrace{x(\nu_1,t_1)}^{\boldsymbol{x}_1} & \cdots & \overbrace{x(\nu_1,t_l)}^{\boldsymbol{x}_l} & \cdots & \overbrace{x(\nu_1,t_N)}^{\boldsymbol{x}_N} \\ \vdots & & \vdots & & \vdots \\ x(\nu_m,t_1) & \cdots & x(\nu_m,t_l) & \cdots & x(\nu_m,t_N) \end{bmatrix} \in \mathbb{R}^{m\times N} \quad (1)$$

whose lth column is the observation sequence $\boldsymbol{x}_l$.

Let now, $\hat{\boldsymbol{\Phi}} = [\hat{\boldsymbol{\varphi}}_1 \ \hat{\boldsymbol{\varphi}}_2 \ \cdots \ \hat{\boldsymbol{\varphi}}_N]$ be a set of functions obtained from the data itself. The POD method allows the data to be represented as a linear combination of functions $\hat{\boldsymbol{\varphi}}_k$ from $\hat{\boldsymbol{\Phi}}$ of the form (a spatio-temporal decomposition) [6]:

$$\boldsymbol{x}_i = \boldsymbol{x}(\nu_j, t_i) = \sum_{k=1}^{N} \boldsymbol{a}_k(t)\hat{\boldsymbol{\varphi}}_k, \quad i = 1, 2, \ldots, l, \ldots N \quad (2)$$

where the index j represents the jth grid (measurement) point, the index i represents the ith snapshot, k represents the statistical or proper orthogonal modes (POD modes), and $a_k(t)$ and $\hat{\boldsymbol{\varphi}}_k$ represent the temporal amplitudes and spatial component maps or patterns (modes), respectively.

Physically, each of these maps represents a standing oscillation, and the temporal coefficients, and $a_k(t_i) = (\hat{\boldsymbol{\varphi}}_k, \boldsymbol{x}_i)$, represent how the patterns oscillate through time, i.e., the temporal coefficients give the relative importance of each mode $\hat{\boldsymbol{\varphi}}_k$ at different moments in time.

Formally, the basis functions are obtained from the solution of the eigenvalue problem

$$\hat{\boldsymbol{C}}\hat{\boldsymbol{\varphi}}_k = \hat{\lambda}_k\hat{\boldsymbol{\varphi}}_k, \quad k = 1, \ldots, N \quad (3)$$

where $\hat{\boldsymbol{C}} = (\boldsymbol{X}_1^N)^T (\boldsymbol{X}_1^N)$ is the spatial covariance matrix and T stands for transpose. The solution of (3) gives a complete set of orthonormal functions $\hat{\boldsymbol{\varphi}}_k$ with corresponding eigenvalues $\hat{\lambda}_1 \geq \hat{\lambda}_2 \geq \cdots \geq \hat{\lambda}_N > 0$. For large-scale applications $m \ll N$, and the method of snapshots is used to reduce the dimension of the system [6], [7].

Using (2), the snapshot matrix, $\boldsymbol{X}_1^N$, can be represented in terms of the POD basis as

$$\boldsymbol{X}_1^N = \hat{\boldsymbol{\Phi}}\hat{\boldsymbol{\Gamma}} \quad (4)$$

where

$$\hat{\boldsymbol{\Gamma}} = \begin{bmatrix} \boldsymbol{a}_1(t) \\ \vdots \\ \boldsymbol{a}_N(t) \end{bmatrix}$$

in which $\boldsymbol{a}_k(t) = [a_k(t_1) \ a_k(t_2) \ \cdots \ a_k(t_N)], k = 1, \ldots, N$ are row vectors containing the temporal coefficients in (2) evaluated at each of the snapshots or observations.

The Appendix discusses extensions to the above approach based on singular value decomposition (SVD) analysis.

B. Koopman Modes

An alternative method to modal analysis of nonlinear complex systems is based on the notion of the Koopman operator [14], [15].

Following Mezic *et al.* [15], consider a discrete-time system evolving on an N-dimensional manifold M

$$\boldsymbol{x}_{k+1} = \boldsymbol{f}(\boldsymbol{x}_k), \quad \boldsymbol{x} \in \mathbb{R}^M \quad (5)$$

$k = 0, 1, 2, \ldots, N-1$ where k is an integer index.

Let $g(\boldsymbol{x}) : M \longrightarrow \mathbb{R}$ be any scalar-valued function (a measurement of the state or observable). The Koopman operator, U, is a a linear operator that maps g into a new function:

$$Ug(\boldsymbol{x}) = g(\boldsymbol{f}(\boldsymbol{x})). \quad (6)$$

The key idea behind Koopman analysis is to study the system dynamics (5), from measured data using the eigenspectrum of U. Assume to this end, that φ_j and λ_j, denote the eigenfunctions and eigenvalues (Koopman modes) of the Koopman operator, respectively, given by

$$U\varphi_j(\boldsymbol{x}) = \lambda_j\varphi_j(\boldsymbol{x}), \quad j = 1, 2, \ldots. \quad (7)$$

where for N sufficiently long, the Koopman eigenfunctions form an orthonormal expansion basis [15].

In practice, one is interested in functions $\boldsymbol{g}(\mathbf{x}) = [g_1(\mathbf{x}) \ g_2(\mathbf{x}) \ \cdots \ g_p(\mathbf{x})] = M \rightarrow p$ with $p < N$. Assuming that each of the components of g lie within the span of the eigenfunctions the time evolution of the functions φ_j the time evolution of the functions $g_1(\mathbf{x}_k)$ can be expanded as

$$\boldsymbol{g}(\boldsymbol{x}) = \sum_{j=1}^{\infty} \varphi_j(\boldsymbol{x})\boldsymbol{v}_j \quad (8)$$

and

$$\boldsymbol{x}_k = \boldsymbol{g}(\boldsymbol{x}_k) = \sum_{J=1}^{\infty} U^k\varphi_j(\boldsymbol{x}_0)\boldsymbol{v}_j = \sum_{J=1}^{\infty} \lambda_j^k\varphi_j(\boldsymbol{x}_0)\boldsymbol{v}_j \quad (9)$$

where use has been made of (7).

Physically, (9) indicates that the observable $\boldsymbol{g}(\boldsymbol{x}_k)$ is decomposed into vector coefficients, $\boldsymbol{v}_j$, called Koopman modes whose temporal behavior is given by the associated eigenvalues λ_j; the phase of the eigenvalues determines its frequency, while its modulus determines the growth rate. The magnitude $\varphi_j(\boldsymbol{x}_0)\boldsymbol{v}_j$ is used as a measure of the relative participation of a mode to the modal decomposition.

This article has been accepted for inclusion in a future issue of this journal. Content is final as presented, with the exception of pagination.

Analytical approaches to compute Koopman modes based on Arnoldi-like algorithms have been developed and tested on data of the form (1). Following the same notation as Susuki and Mezic [10], consider the finite-time data matrix:

$$\boldsymbol{P} = [\,\boldsymbol{P}_0 \quad \boldsymbol{P}_1 \quad \cdots \quad \boldsymbol{P}_{N-1}\,] \in \mathbb{R}^{m\times N} \tag{10}$$

where $g(\boldsymbol{x}_0) = \boldsymbol{P}_0$, and each data column, $\boldsymbol{P}_i$, has a similar interpretation to that in (1).

The computation of the Koopman modes is straightforward [14]:

1) Find constants c_j such that

$$\boldsymbol{r} = \boldsymbol{P}_{N-1} - \sum_{j=0}^{N-2} c_j \boldsymbol{P}_j, \boldsymbol{r} \perp \{\boldsymbol{P}_0 \quad \boldsymbol{P}_1 \quad \cdots \quad \boldsymbol{P}_{N-2}\} \tag{11}$$

2) Determine the eigenvalues (Ritz values) $\lambda_1, \lambda_1, \ldots, \lambda_{N-1}$ of the companion matrix $\boldsymbol{C}$

$$\boldsymbol{C} = \begin{bmatrix} 0 & & & c_o \\ 1 & 0 & & c_1 \\ & \ddots & \ddots & \vdots \\ & & 1\,0 & c_{N-3} \\ & & 1 & c_{N-2} \end{bmatrix} = \boldsymbol{T}^{-1}\Lambda\boldsymbol{T} \in \mathbb{R}^{N-1\times N-1}$$

3) Define the Vandermode matrix

$$\boldsymbol{T} = \begin{bmatrix} 1 & \lambda_1 & \lambda_1^2 & \cdots & \lambda_1^{N-2} \\ 1 & \lambda_2 & \lambda_2^2 & \cdots & \lambda_2^{N-2} \\ 1 & \lambda_3 & \lambda_3^2 & \cdots & \lambda_3^{N-2} \\ \vdots & \vdots & \vdots & \ddots & \vdots \\ 1 & \lambda_{N-1} & \lambda_{N-1}^2 & \cdots & \lambda_{N-1}^{N-2} \end{bmatrix} \in \mathbb{R}^{N-1\times N-1}$$

4) Compute Ritz vectors $\boldsymbol{v}_j$ in (9) as the columns of $\boldsymbol{V} = [\boldsymbol{P}_0\ \boldsymbol{P}_1\ \cdots\ \boldsymbol{P}_{N-2}]\boldsymbol{T}^{-1}$. The Ritz vectors $\boldsymbol{v}_j$ approximate the terms $\varphi_j(x_o)\boldsymbol{v}_j$ in (9).

In this procedure, the constants c_j are determined solving the least-squares problem

$$\boldsymbol{0} = \boldsymbol{b} - \boldsymbol{A}c \tag{12}$$

where $\boldsymbol{c} = [c_o\ \ c_1\ \ c_2\ \ \cdots\ \ c_{N-2}]^{\boldsymbol{T}}$, with $\boldsymbol{b} \in \mathbb{R}^{N-1}$, with $b_i = \boldsymbol{P}_i^T\boldsymbol{P}_{N-1}$ and $\boldsymbol{A} = \{A_{ij}\} \in \mathbb{R}^{(N-1)\times(N-1)}$, with $A_{ij} = \boldsymbol{P}_i^T\boldsymbol{P}_{N-1}$. The Koopman eigenfunctions are obtained from matrix $\boldsymbol{T}$. Refer to [10] for specific details about this procedure.

III. Dynamic Mode Decomposition

A. Background

Dynamic mode decomposition (DMD) is a global multiscale method that can approximate a few Koopman functions φ_j, [16] using two sets of time ordered sequences of data snapshots. More precisely, the method assumes that the data sequences or snapshots, $\boldsymbol{x}_i$, in (1) are generated by a discrete-time linear dynamical system whose evolution is governed by the linear mapping [14]:

$$\boldsymbol{x}_{i+1} = \boldsymbol{A}\boldsymbol{x}_i + \boldsymbol{\eta}_i, \quad i = 1, \ldots, N-1 \tag{13}$$

where $\boldsymbol{A}$ is an unknown (time-independent) operator matrix of dimension $m\times m$ that captures the dynamics inherent in the data matrix, and $\boldsymbol{\eta}_i$ is some noise process. This is a local approximation to system dynamics with a linear system; the eigenvalues and eigenvectors of $\boldsymbol{A}$ determine the dynamic behavior of the mapping.

Practical algorithms to estimate the linear operator $\boldsymbol{A}$ and its associated relevant eigenvalues and eigenvectors that do not require explicit knowledge of the mapping matrix are discussed below.

In the noise-free case, use of (13) in (1) yields the Krylov sequences:

$$\begin{aligned} \boldsymbol{X}_1^N &= [\boldsymbol{x}_1 \quad \boldsymbol{A}\boldsymbol{x}_1 \quad \boldsymbol{A}^2\boldsymbol{x}_1 \quad \cdots \quad \boldsymbol{A}^{N-1}\boldsymbol{x}_1] \\ &= [\boldsymbol{x}_1 \quad \cdots \quad \boldsymbol{x}_N] \qquad (14a) \\ \boldsymbol{X}_1^{N-1} &= [\boldsymbol{x}_1 \quad \boldsymbol{A}\boldsymbol{x}_1 \quad \cdots \quad \boldsymbol{A}^{N-2}\boldsymbol{x}_1] \\ &= [\boldsymbol{x}_1 \quad \cdots \quad \boldsymbol{x}_{N-1}] \qquad (14b) \\ \boldsymbol{X}_2^N &= [\boldsymbol{A}\boldsymbol{x}_1 \quad \boldsymbol{A}^2\boldsymbol{x}_1 \quad \cdots \quad \boldsymbol{A}^{N-1}\boldsymbol{x}_1] \\ &= [\boldsymbol{x}_2 \quad \cdots \quad \boldsymbol{x}_N]. \qquad (14c) \end{aligned}$$

It can be proved that as more vectors $\boldsymbol{x}_{l+1} = \boldsymbol{A}^l\boldsymbol{x}_1, l = 0, \ldots$ are appended, the rank of the Krylov sequences increases until it reaches a maximal value [14]. For a sufficiently large number of snapshots, it can be assumed that the Nth snapshot can be expressed as a linear combination of the previous measurements, i.e.,

$$\boldsymbol{x}_N = c_1\boldsymbol{x}_1 + c_2\boldsymbol{x}_2 + \cdots + c_{N-1}\boldsymbol{x}_{N-1} + \boldsymbol{r} \tag{15}$$

where the c_i's are unknown expansion coefficients, $\boldsymbol{r} \in \mathbb{R}^{m\times 1}$ is a vector of residuals.

Equation (15) can be rewritten in a more useful form as

$$\boldsymbol{x}_N = c_1\boldsymbol{x}_1 + c_2\boldsymbol{x}_2 + \cdots + c_{N-1}\boldsymbol{x}_{N-1} + \boldsymbol{r} = \boldsymbol{X}_1^{N-1}\boldsymbol{c} + \boldsymbol{r}$$

in which $\boldsymbol{c} = [c_1\ \ c_2\ \ c_3\ \ \cdots\ \ c_{N-1}]^{\boldsymbol{T}}$ is a vector of unknown coefficients.

Multiplying (14b) $\boldsymbol{A}$ yields

$$\boldsymbol{A}\boldsymbol{X}_1^{N-1} = \boldsymbol{X}_2^N. \tag{16}$$

It can be easy to shown that the data sequence $\boldsymbol{X}_2^N$ can be expressed as

$$\boldsymbol{X}_2^N = \left[\boldsymbol{x}_2 \quad \boldsymbol{x}_3 \quad \boldsymbol{x}_4 \ \cdots\ \boldsymbol{x}_{N-1}\ \left(\boldsymbol{X}_1^{N-1}\boldsymbol{c}\right)\right] + \boldsymbol{r}\boldsymbol{e}_{N-1} \tag{17}$$

where $\boldsymbol{e}_{N-1} = [0\ \ 0\ \ 0\ \ \cdots\ \ 1] \in \mathbb{R}^{1\times N-1}$ and use has been made of (15).

Further, in matrix form, (16) in connection with (17) can be written as

$$\boldsymbol{X}_2^N = \boldsymbol{A}X_1^{N-1} = \boldsymbol{X}_1^{N-1}\boldsymbol{S} + \boldsymbol{r}\boldsymbol{e}_{N-1} \in \mathbb{R}^{m\times N-1} \tag{18}$$

where

$$\boldsymbol{S} = \begin{bmatrix} 0 & & & c_1 \\ 1 & 0 & & c_2 \\ & \ddots & \ddots & \vdots \\ & & 1\,0 & c_{N-2} \\ & & 1 & c_{N-1} \end{bmatrix} \in \mathbb{R}^{N-1\times N-1} \tag{19}$$

is a *companion* (or Frobenius) *matrix* associated with the DMD method.

This article has been accepted for inclusion in a future issue of this journal. Content is final as presented, with the exception of pagination.

In light of this, the unknown matrix $\boldsymbol{S}$ can be determined by minimizing the residual $\boldsymbol{r}$

$$\boldsymbol{S} = \underbrace{\min}_{\boldsymbol{S}} \left\| \boldsymbol{X}_2^N - \boldsymbol{X}_1^{N-1}\boldsymbol{S} \right\|. \tag{20}$$

A solution to the optimization problem is given by $\boldsymbol{S} = (\boldsymbol{X}_1^{N-1})^{\dagger}\boldsymbol{X}_2^N$, where the notation $(\cdot)^{\dagger}$ denotes the Moore-Penrose pseudo-inverse. Once matrix $\boldsymbol{S}$ is determined, the DMD modes and eigenvalues are obtained by solving the eigenvalue problem $\boldsymbol{S}\boldsymbol{\varphi}_i = \lambda_i\boldsymbol{\varphi}_i, i = 1, \ldots, N-1$. The quality of the estimation can then be computed from (15) and (18) as

$$\|\boldsymbol{r}\| = \left\| \boldsymbol{x}_N - \boldsymbol{X}_1^{N-1}\boldsymbol{c} \right\|.$$

With m being the number of sensors, DMD can be used to obtain low-dimensional spatial decomposition of a high-dimensional transient processes. Let m be the true rank of the data matrix $\boldsymbol{X}_1^{N-1}$. In analogy with POD analysis in Section II (refer to the Appendix), the singular value decomposition (SVD) of matrix $\boldsymbol{X}_1^{N-1}$ is given by

$$\boldsymbol{X}_1^{N-1} = \boldsymbol{U}\boldsymbol{\Sigma}\boldsymbol{W}^T = [\boldsymbol{U}][\boldsymbol{\Sigma}_m \ \boldsymbol{0}] \begin{bmatrix} \boldsymbol{W}_m^T \\ \boldsymbol{W}_s^T \end{bmatrix}, \quad m \ll N \tag{21}$$

where $\boldsymbol{U}$ and $\boldsymbol{W}$ are as defined in the Appendix, and

$$\boldsymbol{\Sigma}_m = \begin{bmatrix} \sigma_1 & \cdots & 0 \\ \vdots & \ddots & \vdots \\ 0 & \cdots & \sigma_m \end{bmatrix}, \quad \sigma_1 \geq \sigma_2 \geq \cdots \geq \sigma_m > 0.$$

A truncated basis can be found by substituting (21) into (18). This yields a reduced model that approximates the original model (19) constructed by projecting onto $\tilde{\boldsymbol{S}}$ the vector field:

$$\tilde{\boldsymbol{X}}_2^N \approx \boldsymbol{A}\boldsymbol{U}\boldsymbol{\Sigma}_m\boldsymbol{W}_m^{\boldsymbol{T}}. \tag{22}$$

Multiplying (22) by $\boldsymbol{U}^T$ from the left and by $\boldsymbol{W}_m\boldsymbol{\Sigma}_m^{-1}$ (from the right), a representation of $\boldsymbol{A}$ in the basis spanned by POD modes of $\tilde{\boldsymbol{X}}_2^N$ is obtained as [17], [18]

$$\tilde{\boldsymbol{S}} \triangleq \boldsymbol{U}^T\boldsymbol{A}\boldsymbol{U} = \boldsymbol{U}^T\tilde{\boldsymbol{X}}_2^N\boldsymbol{W}_m\boldsymbol{\Sigma}_m^{-1} \in \mathbb{R}^{m\times m}. \tag{23}$$

Equation (23) constitutes the reduced companion matrix. Compared to (19), matrix $\tilde{\boldsymbol{S}}$ is of dimension $m \times m, (m \ll N-1)$ and holds information of the modal spatial ($\boldsymbol{U}$) and temporal structures ($\boldsymbol{W}_m\boldsymbol{\Sigma}_m^{-1}$) as discussed below.

B. Modal Decomposition

An interesting interpretation of system dynamic behavior can be obtained from the eigen-decomposition of the low-dimensional system matrix, $\tilde{\boldsymbol{S}}$.

Suppose that matrix $\tilde{\boldsymbol{S}}$ is diagonalizable with eigenvalue decomposition

$$\tilde{\boldsymbol{S}} = \boldsymbol{Y}\boldsymbol{\Lambda}\boldsymbol{Y}^{-1} \tag{24}$$

where $\boldsymbol{\Lambda} = \mathrm{diag}[\lambda_1 \ \lambda_2 \ \cdots \ \lambda_m] \in \mathbb{C}^{m\times m}$ is a diagonal matrix consisting of empirical Ritz eigenvalues λ_j, and $\boldsymbol{Y} = [\boldsymbol{y}_1 \ \boldsymbol{y}_2 \ \cdots \ \boldsymbol{y}_m] \in \mathbb{C}^{m\times m}$ is the matrix of right eigenvectors, respectively.

As discussed above, (24) determines a low-dimensional representation of the mapping $\boldsymbol{A}$ on the subspace spanned by the POD modes of $\boldsymbol{X}_2^N$. Substituting (24) into (23) yields

$$\boldsymbol{U}^T\tilde{\boldsymbol{X}}_2^N\boldsymbol{W}_m\boldsymbol{\Sigma}_m^{-1} = \boldsymbol{Y}\boldsymbol{\Lambda}\boldsymbol{Y}^{-1}. \tag{25}$$

From (25), it is straightforward to show that $\tilde{\boldsymbol{X}}_2^N$ can be approximated using a linear combination of the DMD modes. Multiplying (25) from the left by $\boldsymbol{U}$ and from the right by $\boldsymbol{\Sigma}_m\boldsymbol{W}_m^T$, yields

$$\tilde{\boldsymbol{X}}_2^N \approx \boldsymbol{U}Y\boldsymbol{\Lambda}\boldsymbol{Y}^{-1}\boldsymbol{\Sigma}_m\boldsymbol{W}_m^T. \tag{26}$$

Equation (26) constitutes a reduced-order modal approximation of dimension $m \times N$. Based on this idea, two distinct notions of this decomposition are established.

A first useful interpretation is obtained by inserting (24) in (26):

$$\tilde{\boldsymbol{X}}_2^N \approx \boldsymbol{U}\tilde{\boldsymbol{S}}\boldsymbol{\Sigma}_m\boldsymbol{W}_m^T \approx \boldsymbol{U}\tilde{\boldsymbol{S}}\boldsymbol{\Gamma}_m(t) \tag{27}$$

or

$$\tilde{\boldsymbol{X}}_2^N \approx \begin{bmatrix} \vdots & \vdots & \vdots & \vdots \\ \boldsymbol{u}_1 & \boldsymbol{u}_2 & \cdots & \boldsymbol{u}_m \\ \vdots & \vdots & \vdots & \vdots \end{bmatrix} \begin{bmatrix} \tilde{s}_{11} & \tilde{s}_{12} & \cdots & \tilde{s}_{1m} \\ \tilde{s}_{21} & \tilde{s}_{22} & \cdots & \tilde{s}_{2m} \\ \vdots & \vdots & \ddots & \vdots \\ \tilde{s}_{m1} & \tilde{s}_{m2} & \cdots & \tilde{s}_{mm} \end{bmatrix} \begin{bmatrix} \boldsymbol{a}_1(t) \\ \boldsymbol{a}_2(t) \\ \vdots \\ \boldsymbol{a}_m(t) \end{bmatrix}$$

Upper triangular matrix

Lower triangular matrix

where matrix $\tilde{\boldsymbol{S}}$ is asymmetric with rank $\min(m, N)$, of upper triangular structure and contains a subset of the eigenvalues of $\boldsymbol{A}$.

The following properties can easily be verified:

1) The vectors $\boldsymbol{u}_i$ in matrix $\boldsymbol{U}$ are mutually orthogonal.
2) The m row vector of $\boldsymbol{\Gamma}_m(t)$ are orthogonal, i.e., $\boldsymbol{a}_i(t)\boldsymbol{a}_i^T(t) = \gamma, \boldsymbol{a}_i(t)\boldsymbol{a}_j^T(t) = 0$.
3) In analogy with (2), the temporal vectors $\boldsymbol{a}_i(t)$ are ranked in descending order of energy, i.e., $E_1 > E_2 > \cdots > E_m$, where $E_j = \|\boldsymbol{a}_j(t)\| = \sum_{j=1}^{m}\sigma_j^2$.
4) When matrix $\tilde{\boldsymbol{S}}$ is an mth-order identity matrix, the DMD method reduces to the conventional POD-SVD method in the Appendix.
5) The coefficients of matrix $\tilde{\boldsymbol{S}}$ can be interpreted as weights that calibrate the importance of the temporal structures in determining the system response.

This information is used in this research to determine various measures mode-state participations.

A second interpretation is now obtained in terms of the SVD of the data matrix. Define

$$\boldsymbol{\Phi} \in \mathbb{C}^{m\times m} = \boldsymbol{U}\boldsymbol{Y} = [\boldsymbol{\phi}_1\boldsymbol{\phi}_2 \cdots \ \boldsymbol{\phi}_m]$$

$$\boldsymbol{\Lambda} \in \mathbb{C}^{m\times m} = \begin{bmatrix} \lambda_1 & \cdots & 0 \\ \vdots & \ddots & \vdots \\ 0 & \cdots & \lambda_m \end{bmatrix}$$

and

$$\tilde{\boldsymbol{\Gamma}}_m(t) \in \mathbb{C}^{m\times N-1} = \boldsymbol{Y}^{-1}\boldsymbol{\Sigma}_m\boldsymbol{W}_m^T = \begin{bmatrix} \sum_{k=1}^{m}\hat{\boldsymbol{Y}}_{1k}\boldsymbol{a}_k(t) \\ \vdots \\ \sum_{k=1}^{m}\hat{\boldsymbol{Y}}_{mk}\boldsymbol{a}_k(t) \end{bmatrix} = \begin{bmatrix} \tilde{\boldsymbol{a}}_1(t) \\ \vdots \\ \tilde{\boldsymbol{a}}_m(t) \end{bmatrix}.$$

From the previous discussion, it follows that the estimated data sequence, $\tilde{\boldsymbol{X}}_2^N$, can be expressed as

$$\tilde{\boldsymbol{X}}_2^N \approx \underbrace{\boldsymbol{U}\boldsymbol{Y}}_{\substack{\text{spatial} \\ \text{structure}}} \ \underbrace{\boldsymbol{\Lambda}\boldsymbol{Y}^{-1}\cdot\boldsymbol{\Sigma}_m\cdot\boldsymbol{W}_m^T}_{\substack{\text{Temporal} \\ \text{structure}}} = \boldsymbol{\Phi}\boldsymbol{\Lambda}\tilde{\boldsymbol{\Gamma}}_m(t), \tag{28}$$

This article has been accepted for inclusion in a future issue of this journal. Content is final as presented, with the exception of pagination.

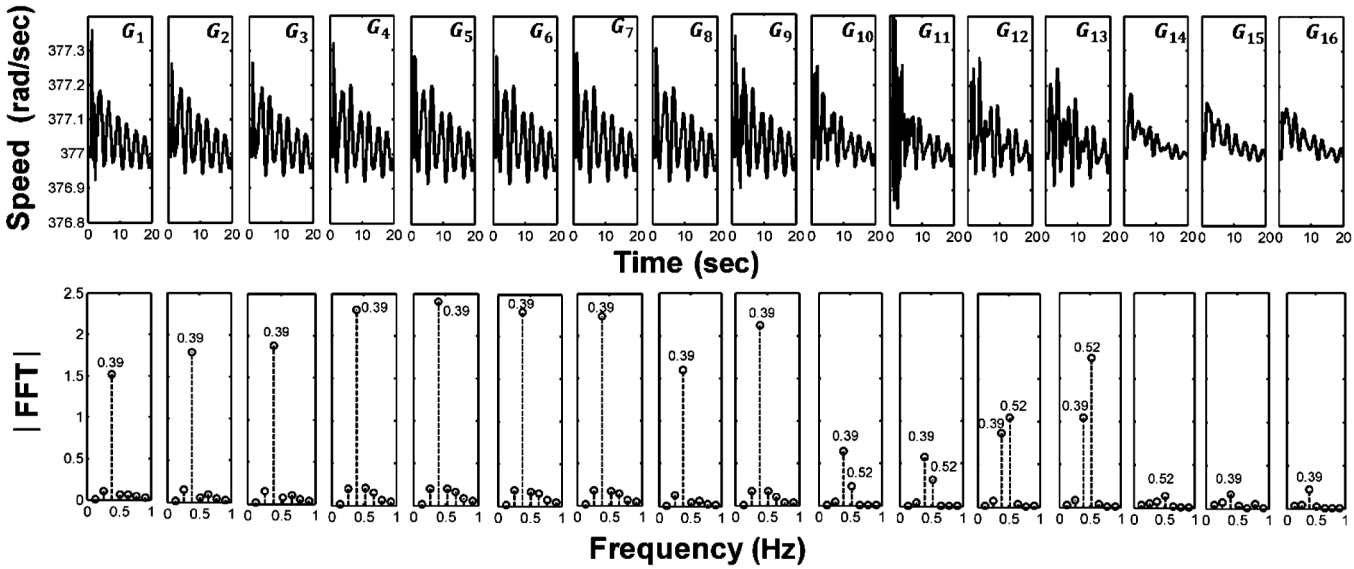

Fig. 1. Machine speed deviations and their associated spectra. (a) Speed. (b) FFT of the signals.

The data matrix $\tilde{\boldsymbol{X}}_2^N$ can be now expanded in a linear combination of modal components as

$$\tilde{\boldsymbol{X}}_2^N \approx \sum_{j=1}^{m} \boldsymbol{\phi}_j \lambda_j \tilde{\boldsymbol{a}}_j(t) \tag{29}$$

where the $\tilde{\boldsymbol{a}}_j$'s are the temporal amplitudes, the $\boldsymbol{\phi}_j$'s are the dynamic or spatial modes (DMD modes), and the λ_j's are the associated frequencies, with

$$\begin{cases} \rho_j = \Re\boldsymbol{e}\{\log(\lambda_j)\}/\Delta t \\ f_j = \Im\boldsymbol{m}\{\log(\lambda_j)\}/\Delta t/2\pi \end{cases} \quad j = 1, 2, \ldots, m. \tag{30}$$

It then follows that the importance of mode j at time t_0 is given by $\|\boldsymbol{\phi}_j\|$, while the phase (mode shape) is given by its phase, $\angle\boldsymbol{\phi}_j$.

Several remarks are in order:

Remark 1: Compared to POD, the modal expansion in (29) decomposes the measured data into a combination of spatio-temporal functions weighted by the corresponding Ritz eigenvalues. Further, the dynamic modes contain additional information concerning the dynamic behavior of the process which is not available from the stationary patterns of the covariance matrix [6], [7].

Compared to the Koopman modal expansions, the DMD modal expansions are of dimension $m \ll N$.

Remark 2: As seen above, the dynamical modes, $\boldsymbol{\phi}_j = \boldsymbol{U}\boldsymbol{y}_j$, corresponding to λ_j, provide the spatial coherent structure (spatial mode shape) of the corresponding oscillatory mode.

IV. Studies on a Small System

A. Test Case and Transient Analysis

As a first illustrative example, the proposed algorithm is applied to the NETS-NYPS test system given in [5]. Datasets of speed deviations and voltage measurements from step-by-step simulations (SBSS) of the nonlinear system model were used to assess the ability of DMD to characterize system behavior.

To allow comparisons with previous studies [12], a ten percent increment of mechanical input torque for 80 ms to each generator was applied. Measurements were recorded over 19 seconds at a rate of 100 samples per second for a total number of 1900 observations.

For the present example, generator speed and bus voltage measurements are used to construct the snapshot matrix (1):

$$\boldsymbol{X}_1^N \in \mathbb{R}^{32\times 1900} = [\boldsymbol{\omega}_1 \ldots \boldsymbol{\omega}_{16} \quad \bar{\boldsymbol{V}}_1 \ldots \bar{\boldsymbol{V}}_{16}]^{\boldsymbol{T}}. \tag{31}$$

Fig. 1 shows the speed deviations of the system generators along with the FFT of the signals. Generators # 1–9, #15, and #16 are seen to have the largest contribution to a dominant mode around 0.39 Hz involving primarily the interaction between machines in areas $\boldsymbol{A}_1$, and areas $\boldsymbol{A}_2$, $\boldsymbol{A}_3$, $\boldsymbol{A}_4$, and $\boldsymbol{A}_5$ [12].

B. Modal Characterization

The NETS-NYPS test system exhibits two electromechanical modes around 0.34 Hz and 0.54 Hz [12] associated with dominant low frequency inter-area modes of oscillation. Studies were conducted to characterize the modal properties of these modes using the DMD method.

Application of the proposed algorithm in Section II-B results in 32 dynamic modes. Fig. 2 shows the normalized or relative energy of each DMD mode, $\hat{\boldsymbol{\sigma}}_k = (\sigma_k^2/\sum_{j=1}^{m}\sigma_j^2)*100$, for the above contingency scenario.

As shown, 6 singular values are seen to capture over 76% of the energy contained in the ensemble of snapshots. In what follows, the relative contribution of these modes to system oscillatory behavior is discussed.

To evaluate the participation of each dynamic mode on the time evolution of measured data, we observe from (28) that

$$\tilde{\boldsymbol{X}}_2^N \approx \begin{bmatrix} \phi_{11} \\ \phi_{21} \\ \vdots \\ \phi_{m1} \end{bmatrix} \lambda_1 \tilde{\boldsymbol{a}}_1(t) + \cdots + \begin{bmatrix} \phi_{1m} \\ \phi_{2m} \\ \vdots \\ \phi_{mm} \end{bmatrix} \lambda_m \tilde{\boldsymbol{a}}_m(t). \tag{32}$$

As shown, each dynamic mode $\boldsymbol{\phi}_j$ is weighted by the product of each Ritz mode value and its corresponding energy extracted from each time-varying mode $\tilde{E}_k = \|\tilde{\boldsymbol{a}}_k(t)\|$.

Using this, we define the state-mode relationship:

This article has been accepted for inclusion in a future issue of this journal. Content is final as presented, with the exception of pagination.

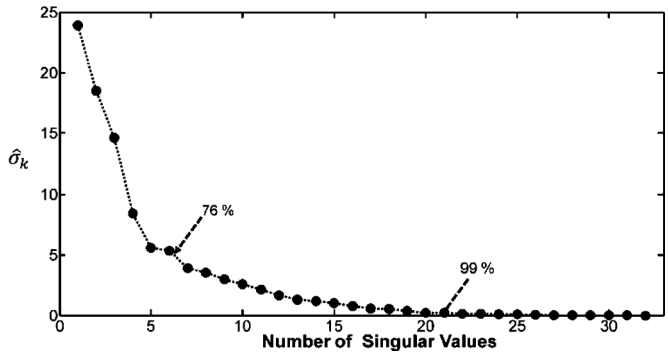

Fig. 2. Relative contribution sum of singular values.

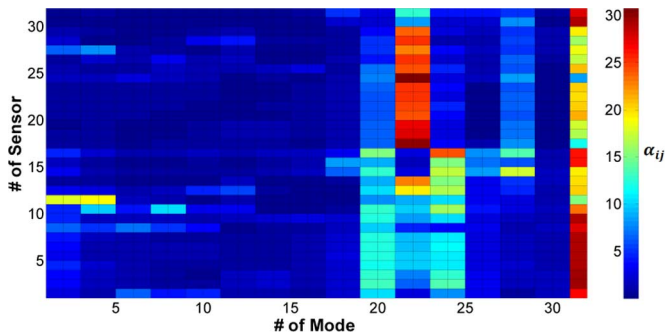

Fig. 3. Participation factor.

$$\tilde{\boldsymbol{X}}_2^N \rightarrow \begin{bmatrix} \alpha_{11} & \overbrace{\alpha_{1j}}^{\lambda_j} & \alpha_{1m} \\ \vdots & \ddots & \vdots \\ \alpha_{m1} & \alpha_{mj} & \alpha_{mm} \end{bmatrix} \tag{33}$$

where the term $\alpha_{ij} = |\phi_{ij}\lambda_j\tilde{E}_j|$ provide a measure of the participation of the jth mode on the system states. Conversely, the columns of (33) provide information about the spatial distribution of modal behavior.

From (33), a spatial (temporal) contribution factor measuring the contribution of each sensor to each state can be defined. The strength of spatial contributions from each sensor to the observed data can be characterized and visualized.

Fig. 3 depicts a 2-D representation of the participation measures in (33) as a function of the sensors' locations.

Examination of Fig. 3 shows that modes # 21 and # 23 are strongly observables at sensors # 18–29, while mode # 31 is observable at most sensors in the system.

Insight into the nature of system behavior can be found by examining the empirical Ritz values, λ and their associated magnitudes [8]. Fig. 4(a) shows a plot of the empirical Ritz values, λ and their associated magnitudes [8]. Fig. 4(a) shows a plot of the empirical Ritz values and their associated energy obtained from the norm of the time-dependent coefficients, $\|\tilde{\boldsymbol{a}}_j(t)\|$, in (29).

For comparison, the Ritz values obtained from Koopman analysis are also included. Fig. 4(b) and (c) show the energy associated with each time-dependent amplitude coefficient.

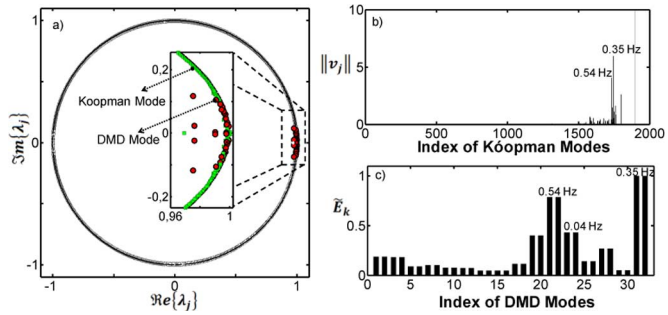

Fig. 4. Empirical Ritz values and their associated norms. (a) Empirical Ritz values estimated by Koopman and DMD, (b) and (c) Norm of dynamic modes and energy amplitudes associated with Koopman and DMD modes.

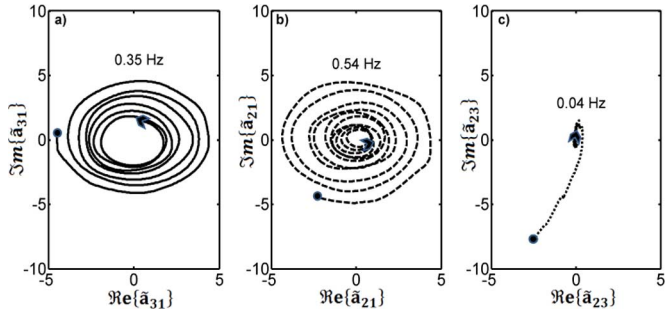

Fig. 5. Phase plane trajectories for the three dominant dynamic modes.

As shown, DMD extracts the most energetic modes (modes associated with intersystem oscillations) whereas Koopman analysis identifies a more general system behavior.

As seen in Fig. 4(a) all the empirical Ritz values are on the unit circle $\|\lambda_j\| \approx 1.0$, indicating that the states of the dynamic system evolve on an attractor. Analysis of the relative energies in Fig. 4(b) and (c), on the other hand, shows that the modes with the largest contributions to the total energy are the 0.35-Hz and 0.54-Hz modes which are associated with the slowest inter-area modes. The third mode at about 0.04-Hz represents the stationary mode of the system.

C. Time-Dependent Amplitude Coefficients

To gain insight into the oscillatory phenomenon, the trajectories associated to the dominant time-varying coefficients identified in Fig. 4(c) were selected for analysis.

Fig. 5 depicts a 2-D visualization of the temporal evolution of the dynamic modes (DMD modes). Examination of these results shows that all selected dynamic modes are evolving in time around an equilibrium condition converging to a stable attractor as expected from the analysis of Ritz values.

The DMD modes associated with the 0.35-Hz and 0.54-Hz modes exhibit the largest amplitudes in agreement with FFT analyses in Fig. 1. In the next section only these dominant modes are analyzed.

D. Identification of Coherent Generator Groups

In order to assess the potential of DMD method, results were compared with the POD method, Koopman analysis and small-signal stability analysis (SSSA) results. Two specific aspects are

This article has been accepted for inclusion in a future issue of this journal. Content is final as presented, with the exception of pagination.

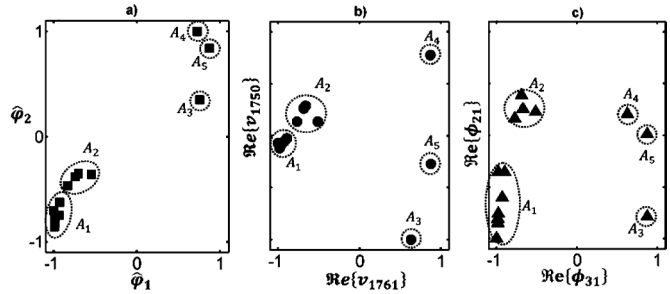

Fig. 6. Comparison of coherency identification method: (a) POD, (b) Koopman, (c) DMD. The areas are defined as $\boldsymbol{G}_1 - \boldsymbol{G}_9$ and areas $\boldsymbol{A}_2(\boldsymbol{G}_{10} - \boldsymbol{G}_{13}), \boldsymbol{A}_3(\boldsymbol{G}_{14}), \boldsymbol{A}_4(\boldsymbol{G}_{15})$ and $\boldsymbol{A}_5(\boldsymbol{G}_{16})$.

of interest to this research: coherency identification and spatial mode shape estimation.

1) Coherency Identification: Clusters of coherent generators can be identified from the spatial signatures of PODs, Koopman and DMs, contained in the modal vectors, $\hat{\varphi}_j$, $\boldsymbol{v}_j$, and $\boldsymbol{\phi}_j$, respectively. Fig. 6 shows scores plots for the two dominant modes obtained using DMD and the POD and Koopman technique described in [7] and [10], respectively. Both techniques identify five groups of coherent generators which correspond to well-defined geographical regions. POD analysis results in less defined groups because of the inability of the method to separate modal components as discussed later in the paper. Further, because phase information is added, the DMD and Koopman analysis naturally allows the analysis of intercluster groupings involving local dynamics.

The coherent groups identified by DMD and Koopman method are in good agreement with results obtained in [12].

2) Mode-Shape Characterization: A key feature of DMD is its ability to incorporate magnitude and phase information. In this section, studies are conducted to evaluate the ability of DMD to extract spatial patterns. Discussion is limited to the two slowest electromechanical modes at about 0.35 Hz and 0.54 Hz.

Based on the complex dynamical modes in $\boldsymbol{\phi}_j$ (29) associated with each dominant mode, the ability of the dynamic decomposition to estimate the mode shapes was computed as in the [8].

The speed spatial mode shape estimates for the 0.35-Hz and 0.54-Hz modes obtained using DMD and SSSA are presented in Fig. 7. At a glance, DMD and Koopman results in Fig. 7 are in qualitative good agreement with SSSA results for the 0.35-Hz mode, although some discrepancies are noted with the results for the 0.54-Hz mode.

Table I compares the modal estimates from DMD with conventional eigenvalue results. Modal damping and frequencies from DMD analysis are found to be in good agreement with SSSA estimates [4].

V. Application to a Large Interconnected System

A7-area, 377-generator transient stability model of the Mexican Interconnected System (MIS) is used to further illustrate the ability of the method to characterize modal behavior. The system model embodies primarily 377 machines represented by detailed two-axis models, 3759 buses, 10 large SVCs, and 2936 branches [7].

Fig. 8 shows a simplified geographical representation of this system illustrating the major transmission and generation facilities and the contingencies selected for study.

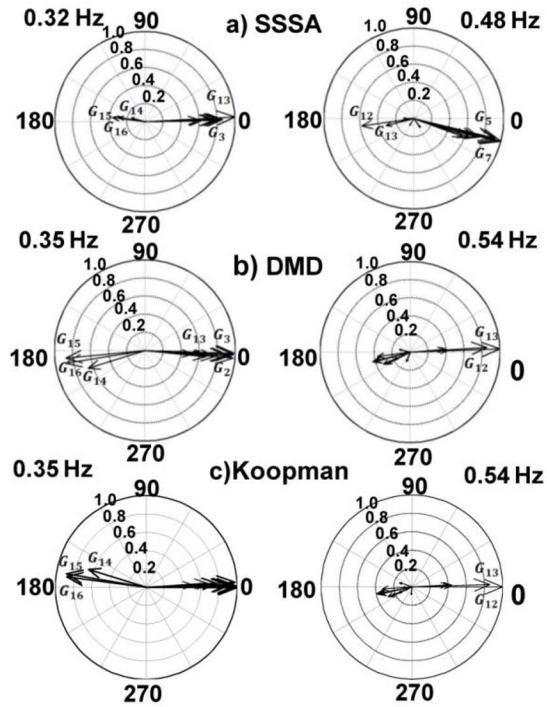

Fig. 7. Mode shape of modes 1 and 2 in Table I showing major coherent groups: (a) SSSA, (b) DMD, (c) Koopman analysis.

TABLE I
Comparison of Modal Estimates

Mode j	*SSSA Frequency* (Hz)	*SSSA Damping*/2π(pu)	*DMD Frequency* (Hz)	*DMD Damping*/2π(pu)
1	**0.321**	**0.027**	**0.352**	**0.024**
2	0.487	0.049	0.547	0.032

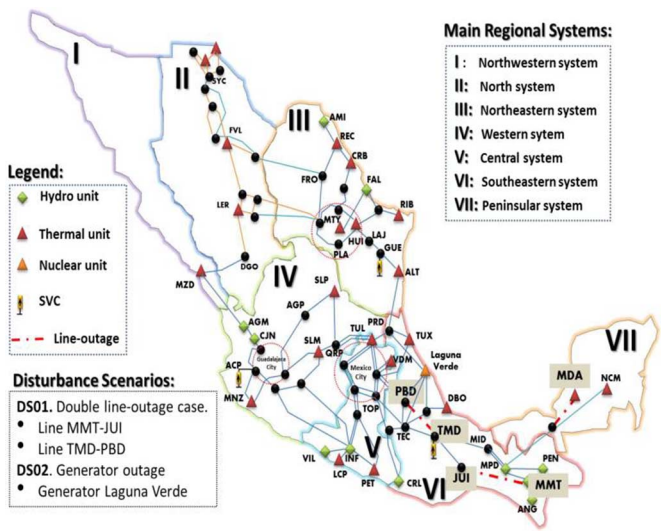

Fig. 8. Schematic of the MIS showing main regional systems and transmission facilities selected for study.

A. System Disturbance Scenarios

The dynamic performance of the 7-area MIS model is governed by four inter-area modes around 0.32 Hz, 0.52 Hz, 0.62 Hz, and 0.78 Hz. Time-domain simulations of selected critical

This article has been accepted for inclusion in a future issue of this journal. Content is final as presented, with the exception of pagination.

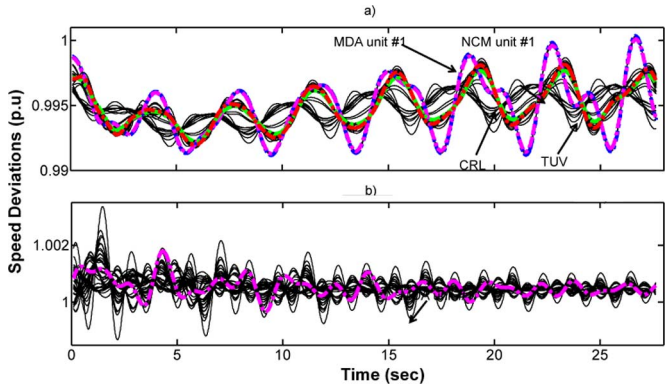

Fig. 9. System dynamic response for scenarios DS01 and DS02.

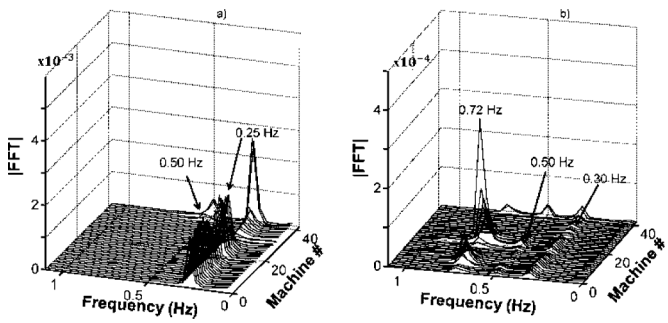

Fig. 10. FFT of the speed deviation of selected generators in Fig. 9. (a) Scenario DS01 and (b) Scenario DS02.

TABLE II
SLOWEST ELECTROMECHANICAL MODES IN THE SYSTEM

Mode j	*Eigenvalue*	*Frequency (Hz)*	*Damping/2π* (pu)	*Oscillation Pattern*
1	-0.022±j2.01	0.32	0.0109	**I,II, III**vs.**IV,V,VI,VII**
2	-0.028±j3.28	0.52	0.0085	**VII** vs.**IV, VI**
3	-0.047±3.91	0.62	0.0109	**II**vs.**III**
4	-0.151±j4.92	0.78	0.0307	**IV** vs. **VI**

disturbances were conducted to test the ability of DMD to characterize the time evolution of these modes.

Following previous studies, two major disturbance events were selected for analysis [7]:

DS01: Double line-outage case. This operating event assumes the simultaneous outage of the 400-kV line from MMT to JUI and the 400-kV line from TMD to PBD on the 400-kV Southeastern-Central interface.

DS02: Generator outage. This scenario assumes the outage, without fault, of Laguna Verde (LGV) power station unit # 1 (650 MW) in the Southeastern system.

These contingencies excite the three slowest swing modes in the system. The transient stability solutions for these cases shown in Fig. 9 were obtained using a time step of 0.0128 s: A 30 second simulation is considered.

In each case, 42 major machines $(m = 42)$ were selected for display and analysis, but the technique can be applied to grids of sensors involving hundreds of simultaneous measurements.

Fig. 10 provides the corresponding spectra while Table II provides a summary description of the four slowest modes in the system identified in the oscillations.

Contingency operating condition DS01 results in unstable oscillations involving the 0.32-Hz mode (interarea mode 1) in which machines in the southeastern (CRL, PEO) and Peninsular systems (NCM, MDA) lose stability as shown in Fig. 9(a). Operating condition DS02, Fig. 9(b), on the other hand, 3 stimulates inter-area modes 1, 2, and 4 in Table II and results in poorly damped oscillations involving most machines in the system.

B. Dynamic Mode Decomposition Analysis

Dynamic mode decomposition was performed on transient stability data in Fig. 9 giving a set of modes which fully characterize system behavior. As discussed above, data was taken at 42 locations; at each location the data was sampled at a rate of 78 samples per second giving a total of 2573 samples. For this analysis, the data matrix is derived from the machine speed deviations arranged as column vectors:

$$\boldsymbol{X}_1^N \in \mathbb{R}^{42\times 2573} = [\Delta\boldsymbol{\omega}_1 \quad \cdots \quad \Delta\boldsymbol{\omega}_{42}]^{\boldsymbol{T}}. \tag{34}$$

The subsequent analysis examines the ability of DMD to assess modal behavior. Comparisons of the performance of the method with Prony analysis, Koopman analysis and POD analysis.

1) Scenario DS01: Fig. 11 shows the speed estimation of the mode shapes associated with the 0.32-Hz mode in Table II extracted using POD, DMD and Koopman analysis. For completeness the time evolution of the time-varying coefficient and its associated spectra are also shown.

Mode shape estimates are in qualitative agreement although some differences are noted. Compared to POD analysis, DMD and Koopman characterization in these plots provides a smoother, more symmetric representation of the 0.32-Hz mode. This, in turn, results in a better characterization and assessment of modal damping and frequency characteristics.

To further verify the suitability of mode decomposition to characterize global behavior, the single-machine (SIME) transient stability method [19] was used to identify the system critical machines relative to the unstable scenario. The method replaces a multimachine system by a one-machine infinite bus (OMIB) system. Fig. 12 displays the OMIB swing curves. To facilitate the analysis, five regional OMIBs are defined corresponding to regional systems II-VII in Fig. 8. Visual inspection of Fig. 12 shows a good agreement with the mode shape results in Fig. 11.

2) Scenario DS02: Scenario DS02 is used to further investigate the applicability of dynamic mode decomposition to characterize multimodal behavior. Based on the preceding results, the analysis focuses on the interarea modes 1, 2 and 4 at 0.32 Hz, 0.52 Hz, and 0.78 Hz, respectively. The time-dependent amplitudes for these modes are shown in Fig. 13 along with their associated spectra. Similar results are obtained using Koopman analysis and are not included here.

These results illustrate several additional advantages (and limitations) of DMD. First, as shown in these plots, DMD effectively decouples transient behavior into essentially single-frequency oscillations, from which modal characteristics can be accurately estimated. In addition, trends and other artifacts are eliminated which has the potential to substantially increase the accuracy and precision of modal estimates. In contrast with this, POD modes are seen to exhibit mode mixing and less regular behavior which makes physical interpretation difficult. The ability of DMD to identify the coherent generators is further illustrated in Fig. 14 which shows the group of coherent generators.

This article has been accepted for inclusion in a future issue of this journal. Content is final as presented, with the exception of pagination.

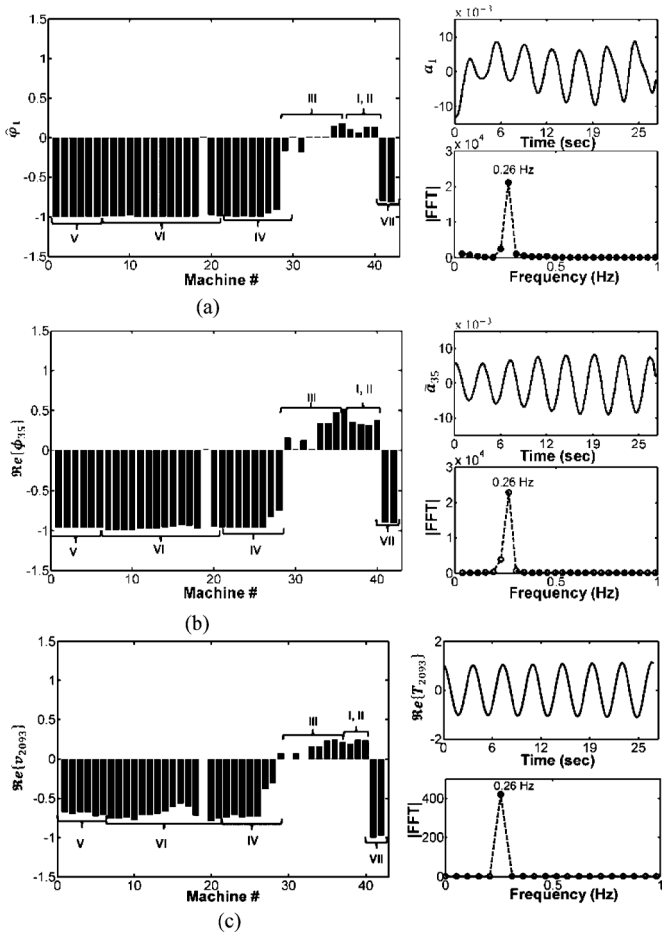

Fig. 11. Mode shapes for the 0.32 Hz mode and its associated temporal coefficient and spectral decomposition computed using (a) POD, (b), DMD, (c) Koopman analysis. Scenario DS01. (a) POD analysis. (b) DMD analysis. (c) Koopman analysis.

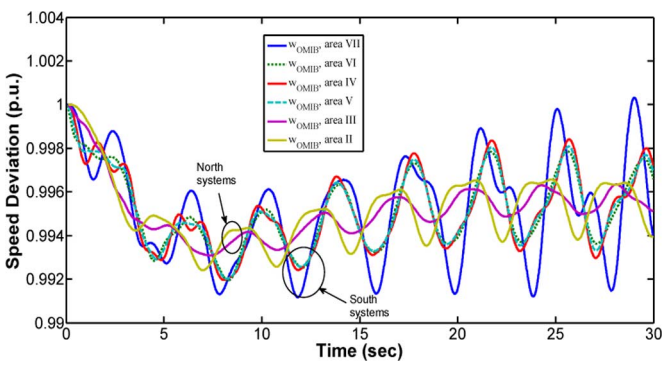

Fig. 12. Time trajectories of the OMIB of the relevant disturbed machine groupings.

Tables III and IV compare DMD estimates with Prony and Koopman mode analyses for scenarios DS01 and DS02 above. Koopman and DMD results are found to be in good agreement while some discrepancies with Prony analysis are noted.

C. Computational Effort

Detailed simulations were conducted to assess the computational needs of DMD analysis for the study of realistic data sets. Table V shows the CPU time needed to characterize system behavior for scenarios DS01 and DS02 above.

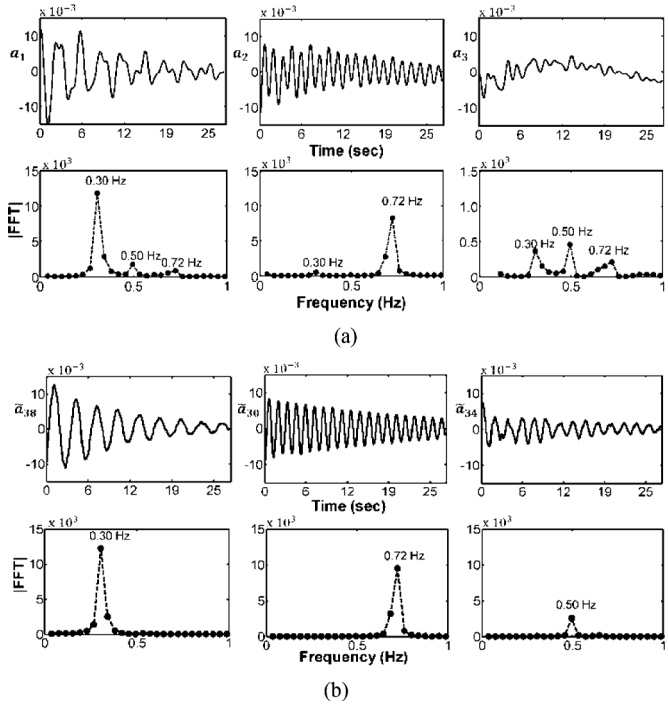

Fig. 13. Time evolution of temporal coefficient and spectral decomposition computed using POD and DMD. Scenario DS02. (a) POD modes. (b) DMD modes.

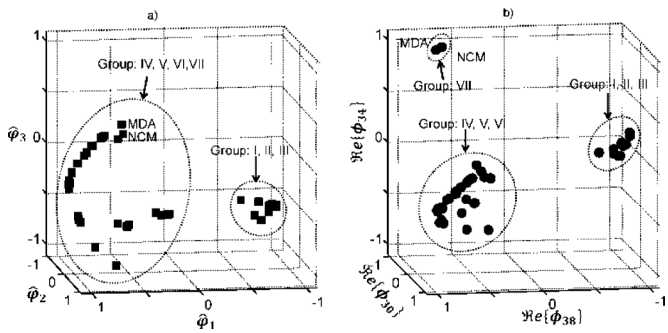

Fig. 14. Comparison of coherency identification methods. (a) POD, (b) DMD. Scenario DS02.

TABLE III
COMPARISON OF MODAL ESTIMATES FOR SCENARIO DS01. TIME WINDOW 0–30 S

Mode	*FFT*	*Prony*		*Koopman*		*DMD***	
	Frequency	*f*	*ξ*	*f*	*ξ*	*f*	*ρ/2π*
1	0.251	0.264 + 0.017* (0.231 -.025)**		0.261	-0.011	0.262	-0.013

* Prony analysis of speed deviations in Fig. 9a
** Prony result for dominant mode on OMIB equivalent in Fig. 12
*** Residue estimate, r=5.3220e-04.

TABLE IV
COMPARISON OF MODAL ESTIMATES FOR SCENARIO DS02. TIME WINDOW 0–30 S

Mode	*FFT*	*Prony*		*Koopman*		*DMD*	
	Frequency	*f*	*ξ*	*f*	*ξ*	*f*	*ρ/2π*
1	0.310	0.316	0.090	0.324	0.097	0.317	0.102
3	0.716	0.722	0.040	0.723	0.041	0.726	0.051

This article has been accepted for inclusion in a future issue of this journal. Content is final as presented, with the exception of pagination.

TABLE V
CPU TIME SIMULATED DATA

Case	*Prony*	*Koopman*	*DMD*	*POD*
DS01	31.54 s	27.49 s	0.491 s	0.050 s
DS02	31.22 s	28.51 s	0.503 s	0.218 s

* CPU time for computation of modal basis

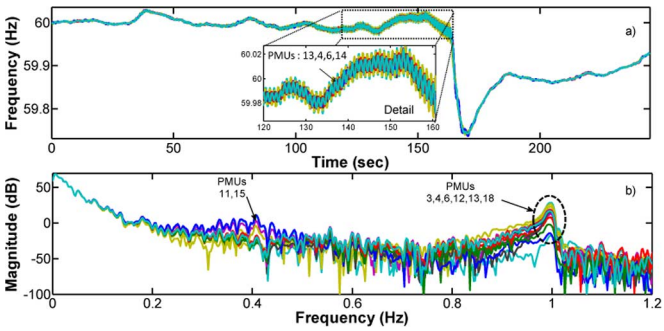

Fig. 15. Time traces of recorded frequency measurements and their associated spectra.

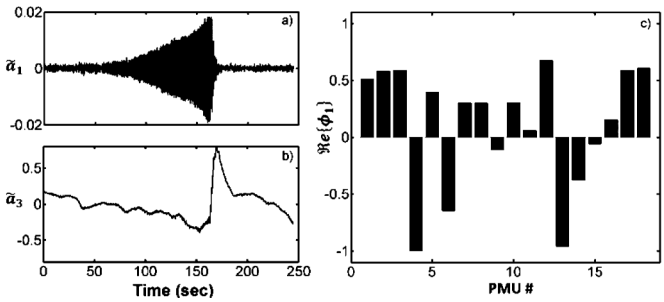

Fig. 16. Spatio-temporal behavior of dominant modes: (a) 0.98 Hz DMD mode 1, (b) DMD mode 3 (collective system behavior), and (c) Mode shape for DMD mode 1.

Results are compared with the Koopman algorithm reported in [10] and a multisignal Prony method [20], based on the Kumaresan-Tuft approach [21] and the OMIB model in Fig. 12.

As shown in Table V, DMD produces accurate enough results with shorter CPU times for both contingency scenarios. The same trend is observed for other operating scenarios.

VI. APPLICATION ON WAMS DATA

Phasor measurement data collected from a real event in the Mexican power system [22] were used to further test the performance of DMD under noisy and nonstationary conditions. Measurements were obtained over a period of 250 seconds at a rate of 20 samples per second. Data were obtained at 18 system locations encompassing 3 major geographical regions [22].

Fig. 15(a) shows selected bus frequency measurements recorded using the CFE wide-area monitoring system (WAMS). Analysis of system behavior in Fig. 16(b) indicates a mode near 0.98 Hz that is strongly observable at PMUs 3, 4, 6, 12, 13, and 18. A second mode near 0.47 Hz is also observable associated with measurements at PMUs 11 and 15.

TABLE VI
MODAL ESTIMATES FOR VARIOUS TECHNIQUES

Time Interval	*FFT*	*Prony*		*Koopman*		*DMD*	
		f	*ξ*	*f*	*ξ*	*f*	*ρ/2π*
0-160 s	1.000	*	*	0.994	-0.015	0.971	-0.029
120-160 s	1.003	1.084	-0.034	0.989	-0.021	0.984	-0.018

* No physically-meaningful solution was obtained

TABLE VII
CPU TIME MEASURED DATA

Time Interval	*Prony*	*Koopman*	*DMD*	*POD*
0-160 s	*	65.35 s	0.457 s	0.104 s
120-160 s	3.73 s	1.395 s	0.430 s	0.099 s

* No physically-meaningful solution was obtained

Application of dynamic mode decomposition analysis results in 18 modes. In the numerical analysis below, the data used is raw data; no preprocessing (detrending, denoising) was applied. Fig. 16 shows the two dominant DMD modes extracted using the procedure in Section II along with the Ritz values. Insight into the nature of these modes can be gleaned in Fig. 16(a) and (b) that show the time evolution of the temporal coefficients $\tilde{\boldsymbol{a}}_j(t)$.

DMD modes 1 and 2 are seen to capture the dominant oscillation at about 0.98 Hz, while mode 3 is a mode associated with the collective motion of all measurements and is equivalent to time-average.

Mode shape analysis results for mode 1 in Fig. 16(c) are found to be in good agreement with the FFT results in Fig. 15(b) and the results in [22] obtained using various techniques.

Table VI compares the modes extracted using DMD with those obtained using Prony analysis and Koopman for two time intervals: 0–160 s (combined ambient and ringdown data) and 120–160 s (ringdown response).

No physically-meaningful results are obtained for the 0–160 s interval using Prony analysis. Table VII shows the CPU times. The accuracy of the compact DMD is demonstrated by its ability produce approximations with residuals smaller than 9.9932e-03.

VII. DISCUSSION AND CONCLUSIONS

This paper has introduced an efficient dynamic mode decomposition technique for modal analysis of large data sets. The method combines the abilities of modal identification techniques such as Prony to extract modal parameters with those of multivariate statistical techniques to isolate and quantify the dominant physical mechanisms.

Experience with simulated data shows that DMD analysis can be efficiently used to analyze large datasets from multiple sources. Several aspects of the theory deserve further investigation including the physical interpretation of dynamic structures, mode-state relationships and the analysis of structural properties of the model. The effect of noise contamination, trends and other artifacts of the dataset and the application to measured data is to be investigated in future research.

This article has been accepted for inclusion in a future issue of this journal. Content is final as presented, with the exception of pagination.

APPENDIX
SVD- BASED PROPER ORTHOGONAL DECOMPOSITION

Alternative approaches to POD analysis based on singular value decomposition of the response matrix (1) have been developed [23]. Singular value decomposition of the data matrix $\boldsymbol{X}_1^N$ in (1) yields

$$\boldsymbol{X}_1^N = \boldsymbol{U}\boldsymbol{\Sigma}\boldsymbol{W}^T = [\boldsymbol{U}][\boldsymbol{\Sigma}_m \quad \boldsymbol{0}] \begin{bmatrix} \boldsymbol{W}_m^T \\ \boldsymbol{W}_s^T \end{bmatrix} \tag{35}$$

where $\boldsymbol{U}$ is an $m \times m$ orthonormal matrix containing the left singular vectors, $\boldsymbol{\Sigma}$ is an $m \times N$ matrix containing the singular values, σ_i, and $\boldsymbol{W}$ is an $N \times N$ matrix containing the right singular vectors.

It can be readily shown, that the proper orthogonal vectors (POMs) defined as the eigenvectors of the covariance matrix $\hat{\boldsymbol{C}}$ in (3) are equal to the left singular values of $\boldsymbol{X}_1^N$; the proper orthogonal vectors (POVs), defined as the eigenvalues λ_i of the covariance matrix, are the squares of the singular values divided by N. The columns of $\boldsymbol{U}$ are the eigenmodes (pseudo mode shapes). Further, the columns $\boldsymbol{w}_i$ of matrix $\boldsymbol{W}$ are the time modulation, $\boldsymbol{a}(t)$ of the modes [23].

REFERENCES

[1] Power System Dynamic Performance Committee, Task Force on Blackout Experience, Mitigation and Role of New TechnologiesP. Kundur and C. Taylor, Chairmen, "Blackout experiences and lessons, best practices for system dynamic performance, and role of new technologies," IEEE Task Force Rep., PES-TR12, 2007.

[2] J. F. Hauer, D. J. Trudnowski, and J. G. DeSteese, "A perspective on WAMS analysis tools for tracking of oscillatory dynamics," in *Proc. IEEE/PES General Meeting*, Tampa, FL, USA, Jun. 2007.

[3] Power System Dynamic Performance Committee, Task Force on Identification of Electromechanical ModesJ. J. Sanchez-Gasca, Chair, "Identification of electromechanical modes in power systems," IEEE/PES, Special Publication TP462, Jun. 2012.

[4] P. Kundur, *Power System Stability and Control*, ser. EPRI Power Engineering Series. New York, NY, USA: McGraw-Hill Professional, 1994.

[5] K. K. Anaparthi, B. Chaudhuri, N. F. Thornhill, and B. C. Pal, "Coherency identification in power systems through principal component analysis," *IEEE Trans. Power Syst.*, vol. 20, no. 3, pp. 1658–1660, Aug. 2005.

[6] P. A. Parrilo, S. Lall, F. Paganini, G. C. Verghese, B. C. Lesieutrez, and J. E. Marsden, "Model reduction for analysis of cascading failures in power systems," ACC99-IEEE0267.

[7] A. R. Messina and V. Vittal, "Extraction of dynamic patterns from wide-area measurements using empirical orthogonal functions," *IEEE Trans. Power Syst.*, vol. 22, no. 2, pp. 682–692, May 2007.

[8] Y. Susuki and I. Mezic, "Nonlinear Koopman modes and coherency identification of coupled swing dynamics," *IEEE Trans. Power Syst.*, vol. 26, no. 4, pp. 1894–1904, Nov. 2011.

[9] Y. Susuki and I. Mezic, "Nonlinear Koopman modes and a precursor to power system swing instabilities," *IEEE Trans. Power Syst.*, vol. 27, no. 3, pp. 1182–1191, Aug. 2012.

[10] Y. Susuki and I. Mezic, "Nonlinear Koopman modes and power stability assessment without models," *IEEE Trans. Power Syst.*, vol. 29, no. 2, pp. 899–907, Mar. 2014.

[11] L. Dosiek, J. W. Pierre, D. J. Trudnowski, and N. Zhou, "A channel matching approach for estimating electromechanical mode shape and coherence," in *Proc. IEEE PES General Meeting*, Jul. 26–30, 2009.

[12] M. A. M. Ariff and B. C. Pal, "Coherency identification in interconnected power system—An independent component," *IEEE Trans. Power Syst.*, vol. 20, no. 2, pp. 1747–1755, May 2012.

[13] D. Yanga, C. Rehtanz, Y. Li, and D. Caib, "Identification of dominant oscillation mode using complex singular value decomposition method," *Elect. Power Syst. Res.*, vol. 83, pp. 227–236, 2012.

[14] C. Rowley, I. Mezic, S. Bagheri, P. Schlatter, and D. Henningson, "Spectral analysis of nonlinear flows," *J. Fluid Mech.*, vol. 641, pp. 115–127, 2009.

[15] I. Mezic, "Analysis of fluid flows via spectral properties of the Koopman operator," *Annu. Rev. Fluid Mech.*, vol. 45, pp. 357–378, 2013.

[16] P. Schmid, "Dynamic mode decomposition of numerical and experimental data," *J. Fluid Mech.*, vol. 656, pp. 5–28, 2010.

[17] P. J. Schmid, D. Violato, and F. Scarano, "Decomposition of time-resolved tomographic PIV," in *ExpFluids*. New York, NY, USA: Springer-Verlag, 2012, vol. 52, pp. 1567–1579.

[18] F. Richecour, L. Hakim, A. Renaud, and L. Zimmer, "DMD algorithm for experimental data processing in combustion," in *Proc. Summer Program Center for Turbulence Research*, 2012, pp. 459–468.

[19] D. Ruiz-Vega, A. R. Messina, and M. Pavella, "Online assessment and control of transients oscillations damping," *IEEE Trans. Power Syst.*, vol. 19, no. 2, pp. 1038–1047, May 2004.

[20] D. J. Trudnowski, J. M. Johnson, and J. F. Hauer, "Making Prony analysis more accurate using multiple signals," *IEEE Trans. Power Syst.*, vol. 14, no. 1, pp. 226–231, Feb. 1990.

[21] D. W. Tufts and R. Kumaresan, "Singular value decomposition and improved frequency estimation using linear prediction," *IEEE Trans. Acoust., Speech, Signal Process.*, vol. ASSP-30, no. 4, pp. 671–675, Aug. 1982.

[22] E. Martinez and A. R. Messina, "Modal analysis of measured inter-area oscillations in the Mexican interconnected system: The July 31, 2008 event," in *Proc. IEEE/PES General Meeting*, Detroit, MI, USA, Jul. 2011.

[23] G. Kerschen, J.-C. Golinval, A. F. Vakakis, and L. A. Bergmann, "The method of proper orthogonal decomposition for dynamical characterization of mechanical systems: An overview," *Nonlin. Dynam.*, vol. 41, pp. 147–169, 2005.

Emilio Barocio (M'99) received the M.E. degree from the University of Guadalajara, Jalisco, Mexico, and the Ph.D. degree from CINVESTAV, Guadalajara, Mexico, in 1998, and 2003, respectively, all in electrical engineering.

Currently, he is an Associate Professor of power systems in the Department of Mechanical and Electrical Engineering, University of Guadalajara.

Bikash C. Pal (M'00–SM'02–F'13) received the B.E.E. (with honors) degree from Jadavpur University, Calcutta, India, the M.E. degree from the Indian Institute of Science, Bangalore, India, and the Ph.D. degree from Imperial College London, London, U.K., in 1990, 1992, and 1999, respectively, all in electrical engineering.

Currently, he is a Professor of power systems in the Department of Electrical and Electronic Engineering, Imperial College London.

Nina F. Thornhill (SM'93) received the B.A. degree in physics from Oxford University, Oxford, U.K., in 1976, the M.Sc. degree from Imperial College London, London, U.K., in 1982, and the Ph.D. degree from University College London in 2005.

Currently, she is a Professor in the Department of Chemical Engineering at Imperial College London where she occupies the ABB/RA Engineering Chair of Process Automation.

Arturo Roman Messina (M'85-SM'05–F'12) received the M.Sc. degree (Honors) in electrical engineering from the National Polytechnic Institute of Mexico, Mexico City, in 1987, and the Ph.D. degree from Imperial College, London, U.K., in 1991.

Since 1997, he has been a Professor at the Center for Research and Advanced Studies (CINVESTAV), Guadalajara, Mexico.

All in-text references underlined in blue are linked to publications on ResearchGate, letting you access and read them immediately.